Utilization of low-concentration coal-bed gas to generate power using a core-shell catalyst-modified solid oxide fuel cell

Xiuqi Yuan [a], Huili Chen [a, *], Wenjuan Tian [a], Jing Shi [d], Wei Zhou [b], Fangqin Cheng [c], Si-Dian Li [a], Zongping Shao [b, e]

[a] Institute of Molecular Science, Key Laboratory of Materials for Energy Conversion and Storage of Shanxi Province, Shanxi University, Taiyuan, 030006, PR China
[b] State Key Laboratory of Materials-Oriented Chemical Engineering, College of Chemical Engineering, Nanjing Tech University, NO.30 Puzhu Road(S), Nanjing, PR China
[c] Institute of Resources and Environmental Engineering, Shanxi University, Taiyuan, PR China
[d] Analytical Instrumentation Center, State Key Laboratory of Coal Conversion, Institute of Coal Chemistry, Chinese Academy of Sciences, 27 South Taoyuan Road, Taiyuan, 030001, PR China
[e] Department of Chemical Engineering, Curtin University, Perth, WA, 6845, Australia

ARTICLE INFO

ABSTRACT

This paper reports a way to utilize low-concentration coal-bed gas(LC-CBG) to generate power using SOFC technology. Ni—BaO—CeO_2@SiO_2 (@NBC) porous nanoparticles with a core-shell structure were synthesized and applied as a protective layer on an anode consisting of Ni—yttria stabilized zirconia (Ni—YSZ). Catalytic activity of @NBC relative to methane partial oxidation was evaluated. Electrochemical performance and durability of the @NBC-modified cells (@NBC//Ni—YSZ) were tested fed with simulated LC-CBG (30% CH_4—70% air). A conventional cell without a protective layer (Ni—YSZ) and a bare NBC-modified cell (NBC//Ni—YSZ) were used for a comparison. The pre- and post-mortem microstructures of cells were analyzed. Influence of porosity of the anode layer on polarization resistance was also investigated. The loading mode of catalysts was discussed as well. Using simulated LC-CBG as a fuel, peak power density of @NBC//Ni—YSZ showed 50% increase at 800 °C comparing with Ni—YSZ at the same conditions. The aging test in galvano-static mode demonstrated good durability of @NBC//Ni—YSZ lasting for over 160 h when exposed to LC-CBG. For comparison, NBC//Ni—YSZ showed rapid voltage drop after 60 h. Voltage of the Ni—YSZ dropped after 10 h. No coking was observed on the @NBC//Ni—YSZ anode surface after the durability tests.

1. Introduction

Solid oxide fuel cells (SOFCs) are very efficient power generation devices with low emission. Among various fuel cells, SOFCs have the advantage of fuel flexibility. Hydrogen as well as coal [1], natural gas [2], syngas [3], other hydrocarbons [4—6], etc. can be used as SOFC fuels. Conventional anode materials for SOFCs are nickel–based cermets, like Ni—YSZ. They have excellent electrical and thermal conductivity as well as electro-catalytic H_2 activity. Ni has high catalytic activity for the cracking of C—H bond. When hydrocarbon complexes are used as a fuel in state-of-art SOFCs, coking on a Ni-based anode occurs causing fast irreversible deterioration of SOFCs [7,8]. Several approaches were suggested to solve coking-induced anode deactivation issues using CH_4-fueled SOFCs. For example, some metals such as Sn, Ru, Cu, Au, Fe, etc. were alloyed with Ni to reduce its catalytic activity for C—H cracking [9—15]. Ni-based anodes can also be modified by additives such as alkaline earth oxides [16—18], CeO_2 [9], etc [19]. Non-nickel-based anodes as potential SOFC anodes were also reported over the past decades [20,21]. However, their performance is still inadequate [22,23]. Both alloying and modifications work at the expense of the activity of the Ni-anode, which lowers fuel utilization.

Internal conversion of hydrocarbons into syngas using O_2, air, CO_2 or H_2O is an effective and a simple approach since Ni is not as susceptible to coking under CO atmosphere comparing to that under CH_4 [24—29]. Low concentration coal bed gas (LC-CBG) from

Nomenclature

NBC	Ni–BaO–CeO$_2$
@ NBC	Ni–BaO–CeO$_2$@SiO$_2$
NOBC	NiO–BaO–CeO$_2$
@ NOBC	NiO–BaO–CeO$_2$@SiO$_2$
LC-CBG	low-concentration coal-bed gas
YSZ	yttria stabilized zirconia
XRD	X-ray diffraction
TEM	Transmission electron microscopy
ICP-MS	Inductively coupled plasma mass spectrometry
PPD	peak power density
SOFC	solid oxide fuel cell
MPO	methane partial oxidation
BSCF	Ba$_{0.5}$Sr$_{0.5}$Co$_{0.8}$Fe$_{0.2}$O$_{3-\delta}$
SDC	Sm$_{0.2}$Ce$_{0.8}$O$_{1.9}$
CTAB	Hexadecyl trimethyl ammonium bromide
EDX	energy dispersive X-ray
SEM	Scanning Electronic Microscopy
EIS	electrochemical impedance spectroscopy

coal-mines contains oxygen. Thus, it causes less coking and it is also a promising natural fuel for SOFC. However, large amount of oxygen-bearing species can oxidize Ni present at the anode [9,30]. Thus, a protective catalytic layer on the surface of a Ni-cermet anode is useful to improve its coking-resistance and antioxidant [19,31–34]. Barnett deposited thin Ru–CeO$_2$ layer on the Ni–YSZ anode surface to convert hydrocarbons into the syngas [35]. In our group, some catalysts, which have moderate catalytic activity for CH$_4$ conversion, such as La$_{0.6}$Sr$_{0.4}$Co$_{0.2}$Fe$_{0.8}$O$_{3-\delta}$ [7] and Sr$_2$Mo-FeO$_{6-\delta}$ [36], were used as independent catalytic layers to facilitate coking-resistance of a Ni-based anode. In this case, development of a very active catalyst for hydrocarbon reforming is very important. Ni-based catalysts attracted a lot of attention because of their low cost, high activity and abundancy as a raw material [37]. However, Ni-based catalysts are more susceptible to sintering comparing to the noble metal catalysts. Sintering of Ni particles leads to the grain growth causing gradual decrease of Ni catalytic activity [38]. Our recent paper [39] demonstrated high catalytic activity of Ni–BaO–CeO$_2$ (NBC) with 13 wt% of Ni toward methane partial oxidation (MPO), CO$_2$ and steam reforming. Using LC-CBG as a fuel, NBC-modified SOFC showed better stability as well as better electrochemical performance comparing to the conventional SOFCs with Ni–yttria stabilized zirconia (YSZ) anodes without the catalytic layer. However, long-term stability still remains an issue. Therefore, sintering-resistance still need to be improved as they are crucial for the stability and catalytic performance of Ni-based catalysts. Catalysts with a core-shell structure have high stability because of the confinement effect of the shell [40,41]. In this paper, porous NBC@SiO$_2$ with a core-shell structure (@NBC with the Ni content equal to 11.5 wt%) is synthesized by incorporating metal oxides into the Ni particles and by coating them with mesoporous SiO$_2$ shell. This material was applied as an anodic protective layer on the Ni–YSZ anode. Based on the confinement effect of the shell, @NBC-modified cell showed good durability for over 160 h using LC-CBG fuel.

2. Experimental section

2.1. Preparation of the catalyst

NiO–BaO–CeO$_2$ (NOBC) samples were synthesized using polymer-assisted combustion method with glucose as a fuel and acrylamide as a dispersing agent. 1.5993 g Ni(NO$_3$)$_2$·6H$_2$O, 0.0856 g Ba(NO$_3$)$_2$ and 5.3626 g Ce(NO$_3$)$_2$·6H$_2$O were dissolved in 200 ml ultra-pure water under constant agitation. C$_6$H$_{12}$O$_6$·H$_2$O and acrylamide were then added one after another. The molar ratio of M^{n+} and glucose versus acrylamide was 1:3:2. Ammonia with the concentration equal to 25 wt % was then added dropwise under constant stirring for pH to be within the 6–10 range. The solution was heated and stirred to facilitate coordination reaction of metal ions until a viscous gel formed. After treatment at 180 °C for 10 h, black porous xerogel formed, which was annealed at 800 °C for 2 h in air.

The prepared method of the core-shell catalyst was referred [42]. 0.464 g of fresh NOBC powder, prepared as described above, was dispersed into 40 ml of water and 120 ml of ethanol. Hexadecyl trimethyl ammonium bromide (CTAB) (0.5g) was then added and the solution was ultra-sonicated for 2 h to obtain clear emulsion. 4 ml of 25 wt% ammonia was added afterwards. Silica source was ethylsilicate (TEOS), 0.25 g of which was dissolved in 40 ml of ethanol, added dropwise into the solution and stirred. Hydrolysis and condensation of the silica precursors were conducted for 2 days at room temperature. Obtained emulsion was centrifuged and rinsed with ethanol twice. The powder was then air dried, after which it was heated at 450 °C for 30 min followed by heating at 700 °C for 4 h (all in air) to remove organics. The resulting product was porous NOBC@SiO$_2$ (@NOBC).

2.2. Fabrication of the single cell

We fabricated NiO–YSZ|YSZ|SDC|BSCF–SDC button cells supported with an anode. NiO and YSZ were purchased from Chengdu Shudu Nanomaterials Technology and Ningbo Institute of Industrial Technology, respectively. Cathode material was Ba$_{0.5}$Sr$_{0.5}$Co$_{0.8}$Fe$_{0.2}$O$_{3-\delta}$ (BSCF), which was synthesized by an EDTA–citrate sol–gel process. Sm$_{0.2}$Ce$_{0.8}$O$_{1.9}$ (SDC) sample was synthesized hydrothermally.

NiO, YSZ, PVB and starch powders (at 6:4:1:0.8 ratio by weight) were ball-milled in ethanol for 1 h at 100 rpm, after which the resulting slurry was dried, ground then sieved with 120-mesh screen to obtain active materials for the anode. 0.43 g of this powder was pressed at 110 MPa for 30 s in a steel mold to create an anode layer. 0.022 g of YSZ powder was then homogeneously spread on the anode layer and the whole assemble was pressed again at 180 MPa forming NiO–YSZ|YSZ bilayer, which was heated 1400 °C for 5 h. The SDC slurry, which was composed of SDC powder and ethylene glycol, was sprayed onto the surface of the YSZ electrolyte. A tri-layer slice of Ni–YSZ|YSZ|SDC was obtained after calcination at 1300 °C for 5 h in air. Thickness of the YSZ and SDC layers was controlled by the amount of powder and spray time, respectively. The total thickness of the electrolyte layer was about 23 μm. Cathode slurry was prepared by mixing BSCF and SDC powder with a 7:3 mass ratio with isopropanol, ethylene glycol and glycerol mixture followed by grinding with a high-energy ball mill at 400 rpm. for 1 h. BSCF–SDC cathode paste was evenly applied on the SDC surface of the tri-layer sample using a spray gun. The final effective cathode area of 0.478 cm^2 was achieved. This assemble was then heated for 2 h at 900 °C. Mixture of silver paste and PVB was smeared on the cathode surface for current collection.

To prepare catalytic slurry, mixture consisting of 0.5 g of the catalyst powder, 0.01 ml of a dispersant and 0.16 g of binders was sprayed onto the external anode layer surface followed by annealing at 700 °C for 1 h. The thickness of the catalyst layer was about 30 μm.

2.3. Electrochemical characterization

Electrochemical testing was performed using Iviumstat electrochemical workstation (Ivium Technologies B.V., Netherlands). Electrochemical impedance spectroscopy was conducted at a 1 MHz - 0.1 Hz frequency range. Before the tests, catalyst and anode layers were in situ reduced under a pure H_2 atmosphere at 700 °C for 2 h. The anode was exposed to the simulated LC-CBG consisting of 30% CH_4 and 70% air introduced into the system at 80 ml min^{-1} flow rate. Cathode was simply surrounded by the ambient air.

2.4. Catalytic assessment

Catalytic activity of @NBC for MPO was evaluated using a fixed-bed reactor at 500–900 °C at ambient pressure. 0.2 g of the catalyst in the grain size range from 250 to 380 μm diluted with 0.8 g of quartz sand in the same grain size range was placed in the middle of the reactor and heated at 800 °C for 2 h to reduce it prior to the reaction. The gas was 30% CH_4–70% air and its flow rate, controlled using flow controllers, was 33 ml min^{-1}. The mixed gas was fed to the reactor, and the effluent gas from the bottom of the reactor gas was guided into an Agilent 7820 gas chromatograph. Considering the high content of O_2 in the fuel gas and the fast kinetic reaction rate of methane oxidation, we assume that CH_4 completely converts to CO and CO_2 without any further products such as coke formation. CH_4 conversion and CO selectivity were calculated as follows:

$$CH_4\ conversion\% = \frac{[CO] + [CO2]}{[CO] + [CO2] + [CH4]} \times 100\%$$

$$CO\ selectivity\% = \frac{[CO]}{[CO] + [CO2]} \times 100\%$$

2.5. Other characterizations

Structures were analyzed using X-ray diffraction (XRD, Rigaku D/Max-RB, Japan) equipped with Cu Kα radiation at $\lambda = 0.1548$ nm. Particle sizes were calculated using Debye–Scherrer equation. TEM images were collected using JEM-2100 instrument operated at 200 kV. For TEM measurements, samples were dispersed in ethanol, sonicated and couple of drops were placed on 400 mesh copper grids pre-coated with carbon film. Morphologies and elemental analysis were characterized by scanning electron microscope (SEM, JSM-7001F, JEOL, Japan) equipped with an energy dispersive X-ray (EDX) spectrometer (Bruker, Germany). The content of Ni in @NBC was analyzed by Inductively coupled plasma mass spectrometry (ICP-MS, NexION 350, PerkinElmer, USA). The porosity of anode layer were detected using mercury intrusion method.

3. Results and discussion

3.1. Crystal structure

Fig. 1 shows XRD patterns of bare NOBC and NBC, SiO_2-encapsuled NOBC (@NOBC) and NBC (@NBC). Bare NOBC consisted of a mixture of fluorite structured CeO_2 (according to the JCPDS card No. 34–0394) and NiO (according to the JCPDS card No.78–0643). The average particle size of CeO_2 and NiO was 16 and 18 nm calculated from the peaks at $2\theta \approx 28.508$ and $43.274°$, respectively. No diffraction peaks that could be attributed to BaO were observed potentially because of its amorphous form [18]. Three small peaks
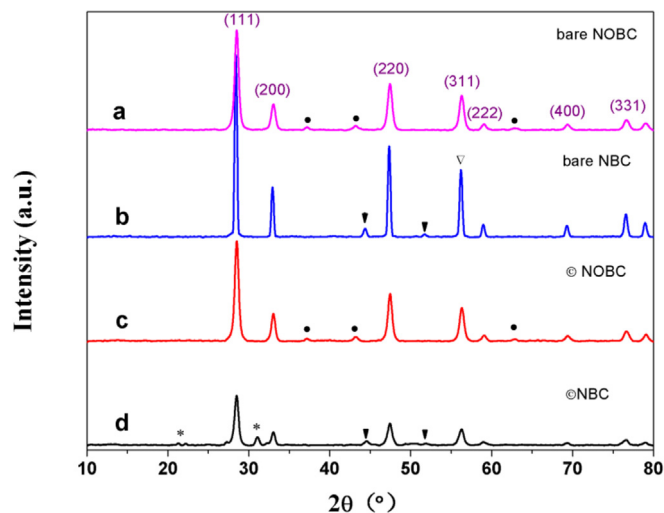

Fig. 1. XRD pattern of catalysts (a) bare NOBC; (b) bare NBC; (c) @NOBC; (d) @NBC.

were observed at 2θ equal to 37.2, 43.2 and 62.8°, which correspond to the 111, 200 and 220 planes of NiO with the rock-salt structure. From the quantities of raw materials we calculated NiO content to be 30.4 mol.%. Low intensity XRD peaks of NiO were either due to the small particle size or dissolution of NiO in CeO_2 lattice [42]. Fig. 1b shows the XRD pattern of the bare NBC. XRD peaks at $2\theta \approx 44.44$ and 51.58° correspond to the metallic Ni resulting from NiO reduction. The average particle size of Ni was 26 nm. The diffraction of CeO_2 at $2\theta \approx 28.51°$ shifted to 28.39°. The average particle size of CeO_2 increases to 31 nm indicating that Ce (IV) was partially reduced within the fluorite structure. @NOBC showed XRD pattern similar to NOBC. No diffraction peak attributed to SiO_2 were observed, which indicates that SiO_2 was in amorphous state. The average particle sizes of CeO_2 and NiO in @NOBC were estimated to be 17.2 nm and 16.8 nm, respectively. @NOBC was reduced to @NBC, and its corresponding XRD pattern is shown in Fig. 1d. A lot of new diffraction peaks appeared comparing to just NBC, which can be attributed to formation of $Ce_{9.33}(SiO_4)_6O_2$ (according to the JCPDS card No.54–0618). Table 1 summarizes data for all four materials. Smaller particle sizes for Ni and CeO_2 were observed for @NBC comparing to the bare NBC indicating that SiO_2 encapsulation prevented coarsening of the particles.

An obvious contrast between dark center and light edges can be seen in the TEM micrograph of the @NOBC calcined at 700 °C (see Fig. 2). The dark areas correspond to NOBC while the surrounding less darker regions correspond to SiO_2 coating. The enlarged view indicates that the NOBC particles are encapsulated by thin SiO_2 layers and the average size of NOBC was 20 nm. The average wall thickness of SiO_2 was about 6 nm, which provided a BET surface area of 15.4 $m^2\,g^{-1}$ with a BJH pore volume of 0.04 $cm^3\,g^{-1}$. Aggregation of NOBC particles, thus, was prevented because of their confinement in the silica shell.

Table 1
Some typical data for all four materials.

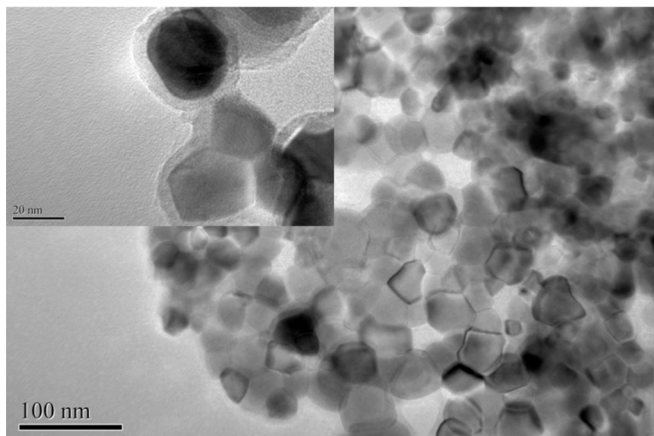|	$2\theta[CeO_2(111)]$	Particle size (nm)	
		NiO or Ni	CeO_2
bare NOBC	28.508	16	18
bare NBC	28.389	26	31
@NOBC	28.548	16.8	17.2
@NBC	28.548	22.6	16

Fig. 2. TEM images of @NOBC.

3.2. Catalytic activity of @NBC for MPO

Theoretically, encapsulation of a catalyst by a porous inert shell will not influence its catalytic activity. Fig. 3a shows @NBC activity for MPO from 500 to 900 °C at 50 °C interval. Simulated LC-CBG (a mixture of 30% CH_4—70% air) with a molar ratio of CH_4/O_2 2:1 was introduced at the top of the tube with a CH_4 10 mL min^{-1} flow rate. CH_4 conversion and CO selectivity increased as the temperature rose. CH_4 conversion below 650 °C was low and the main carbonaceous product was CO_2. CH_4 conversion and CO selectivity increased significantly at temperatures up to 650 °C. Both CO selectivity and CH_4 conversion reached 94% at 850 °C. To prove the catalytic activity of @NBC, a blank experiment without catalyst was conducted under the same conditions. The results demonstrate that CH_4 conversions with high CO selectivity are 3.35, 16.2 and 33.3% at 750, 800 and 850 °C, respectively, which is much lower than those with the catalyst @NBC. Ever Tao et al. reported that when the relative O_2 content as compared to methane was 33%, CH_4 conversion was only about 20% at 900 °C over a blank reactor [43]. High value of the CH_4 conversion demonstrates high catalytic activity of @NBC for MPO. Fig. 3b shows durability of @NBC exposure to 30% CH_4—70% air at 800 °C. It indicates that the catalytic activity was stable over at least 240 h.

3.3. Single cell performance

@NBC-modified cell was used to investigate electrochemical performance, named as "@NBC//Ni—YSZ ". We compared this cell with a conventional one (Ni—YSZ), which did not have a protective layer. All cells were tested using simulated LC-CBG (a mixture of 30% methane—70% air), composition of which is close to the stoichiometric ratio of the MPO reaction. MPO reaction produces H_2 and CO, electrochemically active species to generate power. Values of the peak power densities (PPDs) of temperature-dependent polarization and power outputs of Ni—YSZ were 625, 543, 409, 243 and 110 mW cm^{-2} at 800, 750, 700, 650 and 600 °C, respectively (see Fig. 4a). PPDs of @NBC//Ni—YSZ were 938, 792, 485, 283 and 136 mW cm^{-2} at 800, 750, 700, 650 and 600 °C, respectively (see Fig. 4b). Catalyst-modified cell showed higher performance than the conventional cell at the corresponding temperatures. However, the difference in power output between the two cells became smaller as the temperature dropped below 700 °C. For example, PPDs of Ni—YSZ and @NBC//Ni—YSZ at 650 °C were 243 and 283 mW cm^{-2}, respectively. For the catalyst-modified cell, decreased power output at lower temperatures was observed because of the lower catalytic activity during CH_4 conversion. The low catalytic activity leads to a lower H_2/CO production rate and inadequate fuel supply. Fig. 5a shows performance comparison of @NBC//Ni—YSZ and Ni—YSZ at 800 °C. @NBC//Ni—YSZ demonstrates 50% performance increase comparing to Ni—YSZ. In addition, @NBC//Ni—YSZ showed smaller voltage drop at low current densities indicating lower electrode polarization loss due to the electrochemical reaction of H_2 or CO produced by the @NBC catalyst layer.

The electrochemical impedance spectra (EIS) of @NBC//Ni—YSZ and Ni—YSZ under open circuit condition clearly demonstrated differences in polarization. The ac impedance consists of ohmic as well as electrode polarization resistances. Impedance curve intercept with the real x-axis in the high-frequency region represents overall ohmic resistance (Ro), which combines electronic resistance of the electrodes, ionic resistance of the electrolyte and interface contact resistance. Intercept with the real x-axis at low frequency represents total resistance of the cell. The difference between the values corresponding to the high and low frequency intercepts represents polarization resistance (Rp) associated with electrochemical reactions and mass transfer. As seen in the Nyquist plot shown in Fig. 5b, overall resistances were mainly dominated by the polarization resistance. The two cells showed almost identical ohmic resistance equal to 0.1 Ω cm^2 because they were made from the same materials using the same fabrication process and had the same cell geometry. Thus, different polarization resistance can only be attributed to the anode. @NBC//Ni—YSZ had lower polarization resistance. The up-folded line of @NBC//Ni—YSZ at low frequencies clearly demonstrates a diffusion-controlled process associated with
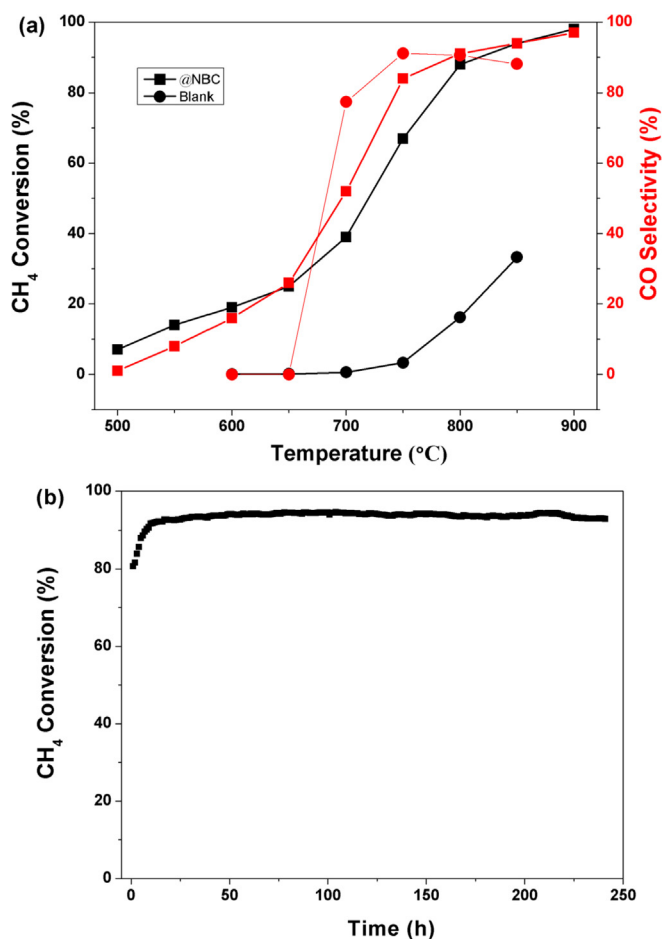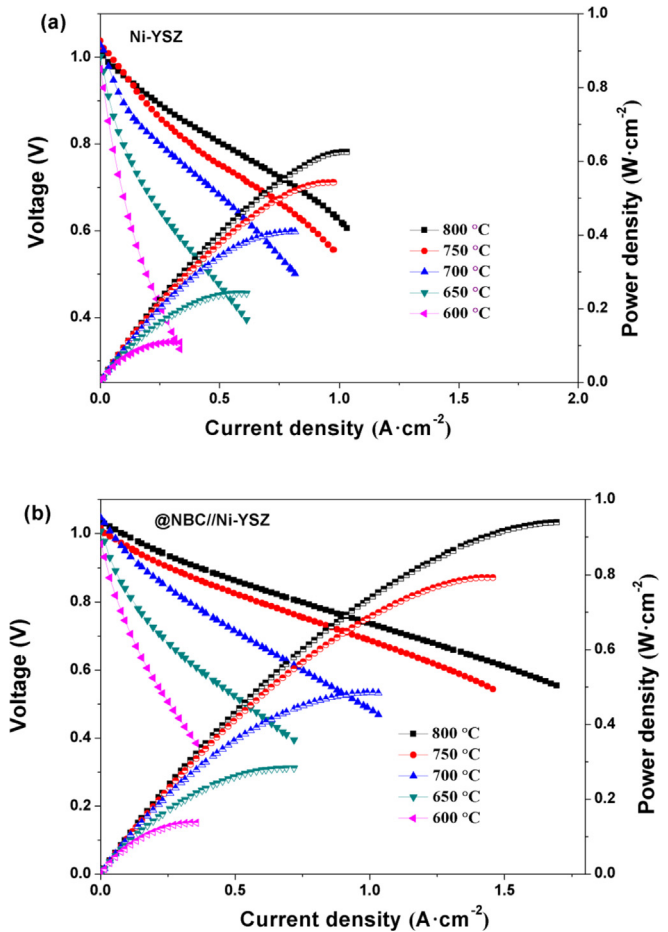

Fig. 3. (a) Catalytic activity of @NBC (■) for 30% CH_4—70% air and a blank experiment (●) without catalyst from 500 °C to 900 °C. (b) Durability of @NBC exposure to 30% CH_4—70% air at 800 °C.

Fig. 4. The I–V(P) curves of Ni–YSZ (a) and @NBC//Ni–YSZ (b) at different temperatures operating on LC-CBG.

Fig. 5. The comparison of I–V(P) (a) and EIS(b) of @NBC//Ni–YSZ and Ni–YSZ at 800 °C operating on LC-CBG.

gas-diffusion, adsorption and dissociation. @NBC particles probably infiltrated the anode layer and blocked some pores on the Ni-cermet anode. The differences in polarization resistance of the two cells can be further studied using Bode plot. With the exception of the region below 1 Hz, the resistances in -Z" direction for @NBC//Ni–YSZ were lower than those for Ni–YSZ at all frequencies. Thus, catalytic layer significantly decreased capacitive resistance. Ni–YSZ showed large capacitance response with the summit frequency at 105 Hz. In addition to the diffusion resistance at low frequencies, @NBC//Ni–YSZ demonstrated a high-frequency characteristic peak at 3158 Hz associated with a charge-transfer process. It is very likely that the coated protective layer blocked some active sites on Ni-cermet anode decreasing its catalytic ability towards H_2 electro-oxidation.

Compared with @NBC//Ni–YSZ, Ni–YSZ exhibited lower electrochemical performance and higher polarization resistance. Probably this is caused by coking on the Ni-cermet anode because the mass content of Ni in the anode is up to 60%. As we know, not only the MPO reaction, Ni is also a good catalyst for the cracking of C–H bond. Without the catalyst barrier layer, CH_4 directly touches with the Ni-cermet anode and reacts at the active Ni sites. Therefore, the reaction in the anode of the cell Ni–YSZ is the balance of CH_4 cracking and MPO reaction.

3.4. Influence of porosity of the anode layer on cell performance

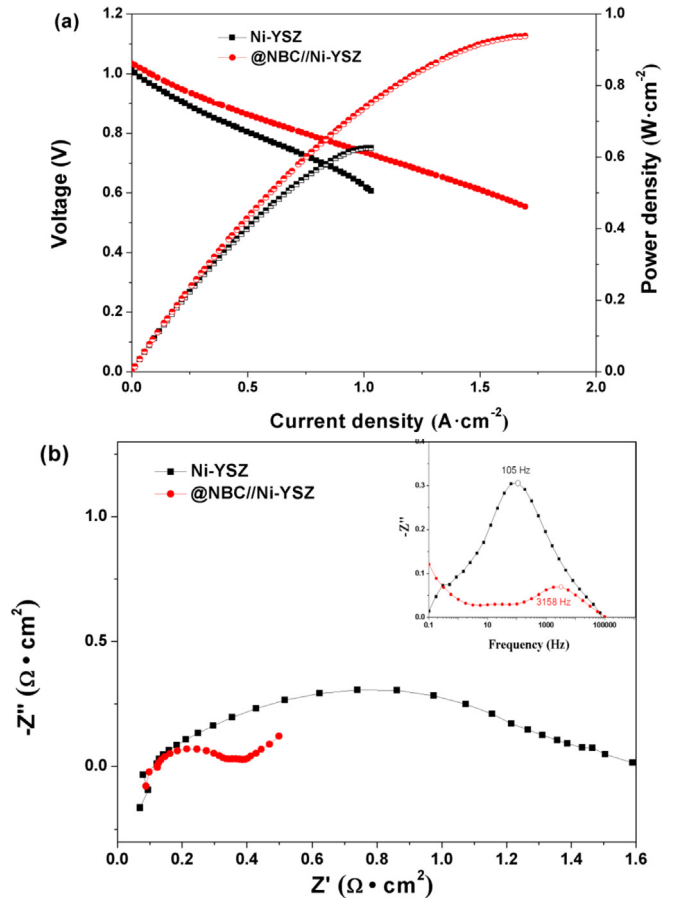From the discussion above, it can be concluded that porosity of

the anode layer has an influence on both diffusion resistance and charge transfer process. To study it further, we prepared an anode layer with 60% porosity using tape casting and incorporated it into a @NBC-modified cell. This cell was named as "@NBC//Ni–YSZ–T". Fig. 6 shows electrochemical performance of @NBC//Ni–YSZ–T at 800 °C operating on LC-CBG. The cell (@NBC//Ni–YSZ), in which the anode/electrolyte bilayer was prepared using co-pressing method, with 38% porosity was used for comparison. @NBC//Ni–YSZ–T delivered 1251 mW cm^{-2} PPD at 800 °C, which is 33% higher comparing with @NBC//Ni–YSZ. To further facilitate this comparison, we subtracted ohmic resistances from the cell impedances. EIS indicates that @NBC//Ni–YSZ–T had smaller polarization resistance than @NBC//Ni–YSZ, no matter for charge transfer resistances at high frequencies or for diffusion resistances at low frequencies. This phenomenon can be explained by higher anode porosity for @NBC//Ni–YSZ–T than for @NBC//Ni–YSZ. Both cells showed an up-folded line at the low frequency region due to the pores blockage by the coated catalyst particles.

3.5. Durability test in galvano-static mode

Durability demonstration is very important to show practicality of the SOFCs. Fig. 7 shows time dependency of the voltage of Ni–YSZ, NBC//Ni–YSZ and @NBC//Ni–YSZ under 200 mA·cm^{-2} current density at 800 °C using LC-CBG as a fuel. It is clear that @NBC//Ni–YSZ showed the best durability with a 0.005 V h^{-1} average degradation rate within 163 h. During the first 12 h, the cell voltage dropped rapidly from 0.84 to 0.75 V,
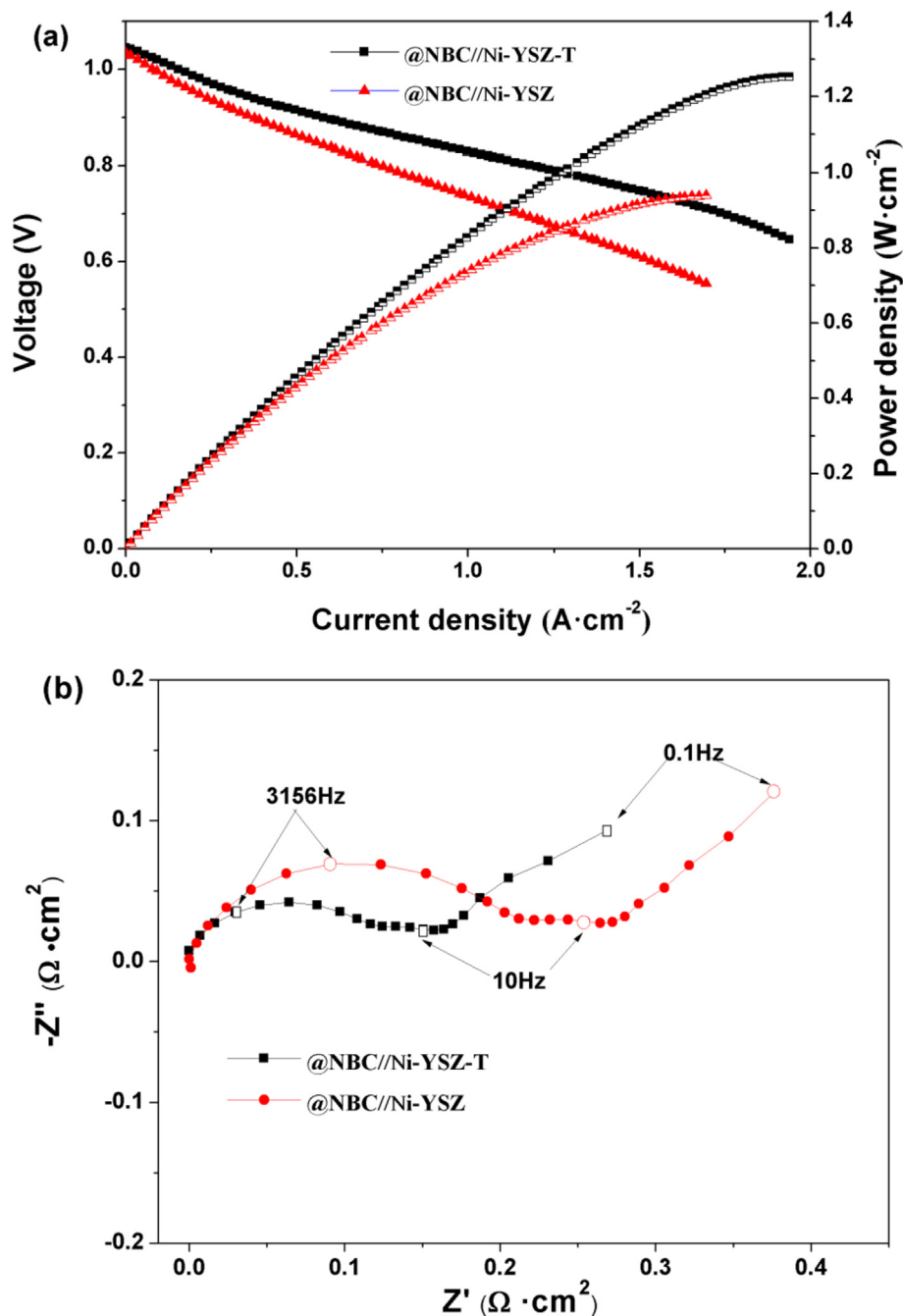
Fig. 6. I−V(P) (a) and ESI (b) of @NBC//Ni−YSZ−T and @NBC//Ni−YSZ at 800 °C operating on LC-CBG.

after which it stabilized. The cell voltage after 163 h was 0.66 V. Cell voltage of the NBC//Ni−YSZ dropped rapidly from 0.84 to 0.70 V during the first 8 h and then gradually decreased to 0.60 V after 60 h. After that, the cell voltage rapidly dropped to 0.1 V indicating severe cell degradation. Voltage of Ni−YSZ dropped from 0.87 V to 0.2 V within 10 h. NBC//Ni−YSZ had similar catalytic activity for MPO with @NBC//Ni−YSZ. The only difference between these two materials was the SiO$_2$ shell. Therefore, the durability of @NBC//Ni−YSZ can be attributed to the confinement effect of the SiO$_2$ shell. The shell prevents active species from sintering at high temperature allowing them to maintain their catalytic activity.

3.6. Morphology characterization

Surface morphologies of the catalyst layers were studied using SEM before and after the durability characterization (Fig. 8). The fresh catalyst surface of a cell which was in situ reduced in the test setup, showed a paper-like fluffy morphology with 72% porosity. After 163 h of the durability test, the catalyst showed some sintering and 57% porosity. Contents of Ni, BaO and CeO$_2$ given by EDX analysis were very consistent with composition of @NBC. Carbon content of the catalyst surface after the durability tests was 11.33 at %, which is close to the carbon content (11.14 at%) of a fresh catalyst surface, indicating good coking-resistance. The source of the carbon
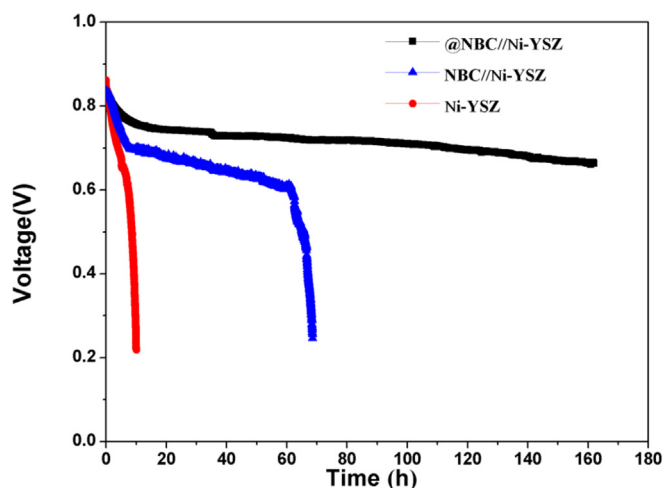
Fig. 7. Time-dependency of the voltage of Ni–YSZ, NBC//Ni–YSZ and @NBC//Ni–YSZ using LC-CBG as a fuel under 200 mA·cm^{-2} current density at 800 °C.
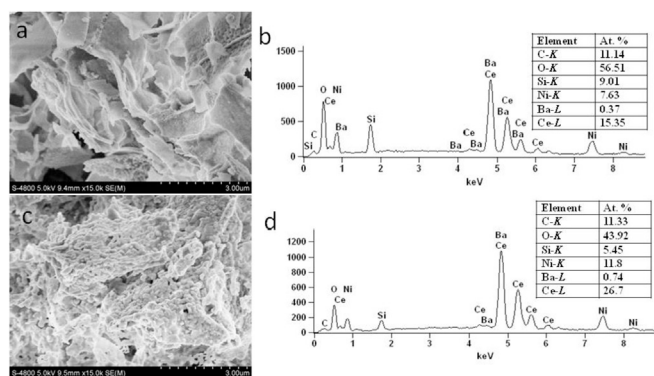

Fig. 8. Surface morphologies and EDX analysis of the catalyst layers before (a, b) and after (c,d) the durability test exposure to LC-CBG.

was probably the residual organic compounds such as dispersant or solvent.

3.7. Catalyst layer loading mode effect on durability

There are two kinds of loading modes for the catalyst layer: indirect and direct modes. For the indirect mode, the catalyst layer is not in contact with the anode layer, as shown in our previous papers [7,40]. In this case, the loaded catalyst layer will not influence the porosity of the anode layer and active sites of the Ni cermet anode. Therefore, the polarization resistance from the anode will not be significantly affected. However, this loading does not work well for a planar-stacked SOFC because stacking between neighboring cells is required. Direct mode is a more suitable planar stacking. However, in this case the coated catalyst particles, especially with small particle sizes, will inevitably infiltrate into the pores of the anode layer and influence fuel diffusion. In addition, the infiltrated catalyst particles can also block some active sites of the Ni cermet anode decreasing anode activity during the electrochemical reaction. In our previous work, using 30% CH$_4$-70% air fuel and NBC as an indirect catalyst layer [39], a stable discharge line for over 55 h was observed without a rapid initial voltage drop. In this work, NBC was directly sprayed on the anode surface using an air brush. Under the same conditions, NBC-modified cell showed a rapid voltage drop in the first 8 h, followed by a gradual voltage

decrease. The difference in the cell stability comes from the different porosity of the catalyst layer. The surface morphologies of the sprayed catalyst layer showed the larger pores, which makes the Ni-cermet anode to be partially exposed. In this case, methane directly reaches the Ni-cermet anode without being pre-reformed, and the cracking occurs. The cracked carbon deposits and blocks the active site of the Ni cermet anode. Therefore, in the infiltration mode, particle sizes and pore sizes of the catalyst layer must be precisely controlled.

4. Conclusions

Our main goal was to improve durability of SOFC with a Ni-cermet anode. A catalyst @NBC with a core-shell framework was prepared. @NBC showed excellent catalytic activity for MPO. The confinement effect of a porous inert shell prevented Ni particles from sintering which provided more active sites. Under SOFC conditions, using simulated LC-CBM fuel, @NBC-modified cell displayed excellent durability, which indicates good coking-resistance. However, there still are some issues to be addressed. For example, particle sizes of a catalyst and porosity of the catalyst layer must be adjusted. Anyway, encapsulation of active catalyst by an inert shell is helpful to improve its thermal stability/sintering-resistance.

References

[1] Y. Jiao, W.J. Tian, H.L. Chen, H.G. Shi, B.B. Yang, C. Li, Z.P. Shao, Z.P. Zhu, S.D. Li, In situ catalyzed Boudouard reaction of coal char for solid oxide-based carbon fuel cells with improved performance, Appl. Energy 141 (2015) 200–208.

[2] F. Santoni, D.M.S. Mosqueda, D. Pumiglia, E. Viceconti, B. Conti, C.B. Munoz, B. Bosio, S. Ulgiati, S.J. McPhail, In-situ study of the gas-phase composition and temperature of an intermediate-temperature solid oxide fuel cell anode surface fed by reformate natural gas, J. Power Sources 370 (2017) 36–44.

[3] T.T. Wan, A.K. Zhu, Y.M. Guo, C.C. Wang, S.G. Huang, H.L. Chen, G.M. Yang, W. Wang, Z.P. Shao, Co-generation of electricity and syngas on proton-conducting solid oxide fuel cell with a perovskite layer as a precursor of a highly efficient reforming catalyst, J. Power Sources 348 (2017) 9–15.

[4] K. Zhao, X.X. Hou, Q. Bkour, M.G. Norton, S. Ha, NiMo-ceria-zirconia catalytic reforming layer for solid oxide fuel cells running on a gasoline surrogate, Appl. Catal. B Environ. 224 (2018) 500–507.

[5] K. Sasaki, I. Takahashi, K. Kuramoto, K. Tomomichi, T. Terai, Reactions on Ni-YSZ cermet anode of solid oxide fuel cells during internal steam reforming of n-octane, Electrochim. Acta 259 (2018) 94–99.

[6] E.K. Park, S. Lee, J.W. Yun, Characteristics of Sr$_{0.92}$Y$_{0.08}$Ti$_{1-y}$NiyO$_{3-\delta}$ anode and Ni-infiltrated Sr$_{0.92}$Y$_{0.08}$TiO$_{3-\delta}$ anode using CH$_4$ fuel in solid oxide fuel cells, Appl. Surf. Sci. 429 (2018) 171–179.

[7] H. Chang, H.L. Chen, Z.P. Shao, J. Shi, J.P. Bai, S.D. Li, In situ fabrication of (Sr, La)FeO$_4$ with CoFe alloy nanoparticles as an independent catalyst layer for direct methane-based solid oxide fuel cells with a nickel cermet anode, J. Mater. Chem. A 4 (2016) 13997–14007.

[8] W. Wang, C. Su, Y.Z. Wu, R. Ran, Z.P. Shao, Progress in solid oxide fuel cells with nickel-based anodes operating on methane and related fuels, Chem. Rev. 113 (2013) 8104–8151.

[9] G. Chen, G.Q. Guan, S. Abliz, Y. Kasai, A. Abudula, Rapid degradation phenomenon of NiCu-Ce$_{0.8}$Gd$_{0.2}$O$_{1.9}$ anode at high p(H$_2$O) in different concentrations of dry methane, Electrochim. Acta 56 (2011) 9868–9874.

[10] J.H. Myung, S.D. Kim, T.H. Shin, D. Lee, J.T.S. Irvine, J. Moon, S.H. Hyun, Nano-composite structural Ni-Sn alloy anodes for high performance and durability of direct methane-fueled SOFCs, J. Mater. Chem. 3 (2015) 13801–13806.

[11] F.J. Garcia-Garcia, F. Yubero, A.R. Gonzalez-Elipe, R.M. Lambert, Microstructural engineering and use of efficient poison resistant Au-doped Ni-GDC ultrathin anodes in methane-fed solid oxide fuel cells, Int. J. Hydrogen Energy 43 (2018) 885–893.

[12] Y. Yoon, H. Kim, J. Lee, Enhanced catalytic behavior of Ni alloys in steam

methane reforming, J. Power Sources 359 (2017) 450–457.

[13] Z.C. Wang, S.Q. Wang, S.Y. Jiao, W.J. Weng, K. Cheng, B. Qian, H.L. Yu, Y.M. Chao, A hierarchical porous microstructure for improving long-term stability of Ni$_{1-x}$Cu$_x$/SDC anode-supported IT-SOFCs fueled with dry methane, J. Alloy. Comp. 702 (2017) 186–192.

[14] J.C. Li, Y. Yu, Y.M. Yin, N. Zhou, Z.F. Ma, A novel high performance composite anode with in situ growth of Fe-Ni alloy nanoparticles for intermediate solid oxide fuel cells, Electrochim. Acta 235 (2017) 317–322.

[15] N. Wu, W. Wang, Y.J. Zhong, G.M. Yang, J.F. Qu, Z.P. Shao, Nickel-Iron alloy nanoparticle-decorated K$_2$NiF$_4$-type oxide as an efficient and sulfur-tolerant anode for solid oxide fuel cells, Chemelectrochem 4 (2017) 2378–2384.

[16] J.F. Qu, W. Wang, Y.B. Chen, X. Deng, Z.P. Shao, Stable direct-methane solid oxide fuel cells with calcium-oxide-modified nickel-based anodes operating at reduced temperatures, Appl. Energy 164 (2016) 563–571.

[17] M.D. McIntyre, J.D. Kirtley, A. Singh, S. Islam, J.M. Hill, R.A. Walker, Comparing in situ carbon tolerances of Sn-infiltrated and BaO-infiltrated Ni-YSZ cermet anodes in solid oxide fuel cells exposed to methane, J. Phys. Chem. C 119 (2015) 7637–7647.

[18] Y.F. Song, W. Wang, L. Ge, X.M. Xu, Z.B. Zhang, P. Sergio, B. Juliao, W. Zhou, Z.P. Shao, Rational design of a water-storable hierarchical architecture decorated with amorphous barium oxide and nickel nanoparticles as a solid oxide fuel cell anode with excellent sulfur tolerance, Adv. Sci. 4 (2017).

[19] X.L. Yao, L.J. Fan, T. Gan, N.J. Hou, P. Li, Y.C. Zhao, Y.D. Li, Coking-resistant NbO$_x$-Ni-Ce$_{0.8}$Sm$_{0.2}$O$_{1.9}$ anode material for methanol-fueled solid oxide fuel cells, Int. J. Hydrogen Energy 43 (2018) 12748–12755.

[20] M.K. Rath, K.T. Lee, Characterization of novel Ba$_2$LnMoO$_6$ (Ln = Pr and Nd) double perovskite as the anode material for hydrocarbon-fueled solid oxide fuel cells, J. Alloy. Comp. 737 (2018) 152–159.

[21] P. Kumar, S. Presto, A.S.K. Sinha, S. Varma, M. Viviani, P. Singh, Effect of samarium (Sm^{3+}) doping on structure and electrical conductivity of double perovskite Sr$_2$NiMoO$_6$ as anode material for SOFC, J. Alloy. Comp. 725 (2017) 1123–1129.

[22] B.B. Niu, F.J. Jin, X. Yang, T. Feng, T.M. He, Resisting coking and sulfur poisoning of double perovskite Sr$_2$TiFe$_{0.5}$Mo$_{0.5}$O$_{6-\delta}$ anode material for solid oxide fuel cells, Int. J. Hydrogen Energy 43 (2018) 3280–3290.

[23] N. Zhou, Y.M. Yin, Z.H. Chen, Y.F. Song, J.W. Yin, D. Zhou, Z.F. Ma, A regenerative coking and sulfur resistant composite anode with Cu exsolution for intermediate temperature solid oxide fuel cells, J. Electrochem. Soc. 165 (2018) F629–F634.

[24] M. Pillai, Y.B. Lin, H.Y. Zhu, R.J. Kee, S.A. Barnett, Stability and coking of direct-methane solid oxide fuel cells: effect of CO$_2$ and air additions, J. Power Sources 195 (2010) 271–279.

[25] H. Sumi, T. Yamaguchi, H. Shimada, Y. Fujishiro, M. Awano, Internal partial oxidation reforming of butane and steam reforming of ethanol for anode-supported microtubular solid oxide fuel cells, Fuel Cells 17 (2017) 875–881.

[26] M. Li, B. Hua, J.L. Luo, Alternative fuel cell technologies for cogenerating electrical power and syngas from greenhouse gases, ACS Energy Lett. 2 (2017) 1789–1796.

[27] D. Lee, J. Myung, J. Tan, S.H. Hyun, J.T.S. Irvine, J. Kim, J. Moon, Direct methane solid oxide fuel cells based on catalytic partial oxidation enabling complete coking tolerance of Ni-based anodes, J. Power Sources 345 (2017) 30–40.

[28] Q. Bkour, K. Zhao, L. Scudiero, D.J. Han, C.W. Yoon, O.G. Marin-Flores, M.G. Norton, S. Ha, Synthesis and performance of ceria-zirconia supported Ni-Mo nanoparticles for partial oxidation of isooctane, Appl. Catal. B Environ. 212 (2017) 97–105.

[29] T. Herrmann, M. Dillig, M. Hauth, J. Karl, Conversion of tars on solid oxide fuel cell anodes and its impact on voltages and current densities, Energy Sci. Eng. 5 (2017) 194–207.

[30] G. Chen, G.Q. Guan, Y. Kasai, H.X. You, A. Abudula, Degradation mechanism of Ni-based anode in low concentrations of dry methane, J. Power Sources 196 (2011) 6022–6028.

[31] M. Lo Faro, R.M. Reis, G.G.A. Saglietti, V.L. Oliveira, S.C. Zignani, S. Trocino, S. Maisano, E.A. Ticianelli, N. Hodnik, F. Ruiz-Zepeda, A.S. Aricò, Solid oxide fuel cells fed with dry ethanol: the effect of a perovskite protective anodic layer containing dispersed Ni-alloy @ FeO$_x$ core-shell nanoparticles, Appl. Catal. B Environ. 220 (2018) 98–110.

[32] C.A. Thieu, J. Hong, H. Kim, K.J. Yoon, J.H. Lee, B.K. Kim, J.W. Son, Incorporation of a Pd catalyst at the fuel electrode of a thin-film-based solid oxide cell by multi-layer deposition and its impact on low-temperature co-electrolysis, J. Mater. Chem. 5 (2017) 7433–7444.

[33] W. Wang, F. Wang, Y.B. Chen, J.F. Qu, M.O. Tade, Z.P. Shao, Ceramic lithium ion conductor to solve the anode coking problem of practical solid oxide fuel cells, Chemsuschem 8 (2015) 2978–2986.

[34] J. Zhao, X.Y. Xu, W. Zhou, I. Blakey, S.M. Liu, Z.H. Zhu, Proton-conducting La-doped ceria-based internal reforming layer for direct methane solid oxide fuel cells, ACS Appl. Mater. Interfaces 9 (2017) 33758–33765.

[35] Z.L. Zhan, S.A. Barnett, An octane-fueled olid oxide fuel cell, Science 308 (2005) 844–847.

[36] H.L. Chen, F. Wang, W. Wang, D.F. Chen, S.D. Li, Z.P. Shao, H$_2$S poisoning effect and ways to improve sulfur tolerance of nickel cermet anodes operating on carbonaceous fuels, Appl. Energy 179 (2016) 765–777.

[37] M. Aghayan, D.I. Potemkin, F. Rubio-Marcos, S.I. Uskov, P.V. Snytnikov, I. Hussainova, Template-assisted wet-combustion synthesis of fibrous nickel-based catalyst for carbon dioxide methanation and methane steam reforming, ACS Appl. Mater. Interfaces 9 (2017) 43553–43562.

[38] F.S. da Silva, T.M. de Souza, Novel materials for solid oxide fuel cell technologies: a literature review, Int. J. Hydrogen Energy 42 (2017) 26020–26036.

[39] H.L. Chen, Y.F. Wu, G.M. Yang, J. Shi, W. Zhou, J.P. Bai, S.D. Li, Z.P. Shao, Direct power generation from low concentration coal-bed gas by a catalyst-modified solid oxide fuel cell, Chemelectrochem 5 (2018) 1459–1466.

[40] A.J. Majewski, J. Wood, Tri-reforming of methane over Ni@SiO$_2$ catalyst, Int. J. Hydrogen Energy 39 (2014) 12578–12585.

[41] J.L. Pu, K. Nishikado, N.N. Wang, T.T. Nguyen, T. Maki, E.W. Qian, Core-shell nickel catalysts for the steam reforming of acetic acid, Appl. Catal. B Environ. 224 (2018) 69–79.

[42] L. Barrio, A. Kubacka, G. Zhou, M. Estrella, A. Martinez-Arias, J.C. Hanson, M. Fernandez-Garcia, J.A. Rodriguez, Unusual physical and chemical properties of Ni in Ce$_{1-x}$Ni$_x$O$_{2-y}$ oxides: structural characterization and catalytic activity for the water gas shift reaction, J. Phys. Chem. C 114 (2010) 12689–12697.

[43] S.W. Tao, J.T.S. Irvine, S.M. Plint, Methane oxidation at redox stable fuel cell electrode La$_{0.75}$Sr$_{0.25}$Cr$_{0.5}$Mn$_{0.5}$O$_{3-\delta}$, J. Phys. Chem. B 110 (2006) 21771–21776.